

# Large Bulk Photovoltaic Effect and Spontaneous Polarization of Single-Layer Monochalcogenides

Tonatiuh Rangel,<sup>1,2,\*</sup> Benjamin M. Fregoso,<sup>2,3,\*</sup> Bernardo S. Mendoza,<sup>4</sup> Takahiro Morimoto,<sup>2</sup> Joel E. Moore,<sup>2</sup> and Jeffrey B. Neaton<sup>1,2,5</sup>

<sup>1</sup>*Molecular Foundry, Lawrence Berkeley National Laboratory, Berkeley, California 94720, USA*

<sup>2</sup>*Department of Physics, University of California, Berkeley, California 94720, USA*

<sup>3</sup>*Department of Physics, Kent State University, Kent, Ohio 44242, USA*

<sup>4</sup>*Centro de Investigaciones en Óptica, León, Guanajuato 37150, México*

<sup>5</sup>*Kavli Energy Nanosciences Institute at Berkeley, Berkeley, California 94720, USA*

We use a first-principles density functional theory approach to calculate the shift current and linear absorption of uniformly illuminated single-layer Ge and Sn monochalcogenides. We predict strong absorption in the visible spectrum and a large effective three-dimensional shift current ( $\sim 100 \mu\text{A}/\text{V}^2$ ), larger than has been previously observed in other polar systems. Moreover, we show that the integral of the shift-current tensor is correlated to the large spontaneous effective three-dimensional electric polarization ( $\sim 1.9 \text{ C}/\text{m}^2$ ). Our calculations indicate that the shift current will be largest in the visible spectrum, suggesting that these monochalcogenides may be promising for polar optoelectronic devices. A Rice-Mele tight-binding model is used to rationalize the shift-current response for these systems, and its dependence on polarization, in general terms with implications for other polar materials

*Introduction.*— The shift current is a dc current generated in a material under uniform illumination [1–4], and gives rise to phenomena such as the bulk photovoltaic effect (BPVE) [1]. A necessary condition for the BPVE in a material is the lack of inversion symmetry. Interestingly, in the BPVE, the resulting photovoltage is not limited by the band gap energy, and a junction or interface is not required to generate a current. These properties of the BPVE motivate great interest in the possible optoelectronic applications of noncentrosymmetric systems, and they have been suggested to play a role in emerging functional materials, including hybrid halide perovskites [5].

The BPVE is much less studied in two-dimensional (2D) materials [6–8]. Two-dimensional materials represent the ultimate scaling in thickness with mechanical, optical, and electronic properties that are unique relative to their bulk counterparts. For example, single-layer group-IV monochalcogenides GeS, GeSe, SnS, and SnSe are actively being investigated [9–17] due to their band gaps and large carrier mobilities suitable for optoelectronics. Centrosymmetric in the bulk, the monochalcogenides lack inversion symmetry in single-layer form, allowing for the emergence of a spontaneous polarization and a BPVE. Although broken inversion symmetry is necessary for a nonzero shift current, the relationship between shift current and polarization at a given frequency is complex and depends on the degree of asymmetry and spatial localization of the valence and conduction states [5]. On the other hand, the shift-current spectrum integrated over frequency is clearly correlated to polarization, as shown in this Letter. In this Letter we use first principles density functional theory methods, supplemented by a tight-binding model, to predict and understand the spontaneous polarization and BPVE in single-layered monochalcogenides. In

addition to confirming their established favorable band gaps and strong absorption [18, 19], we demonstrate that the monochalcogenides exhibit a large in-plane shift current, up to  $100 \mu\text{A}/\text{V}^2$ . Using a Rice-Mele tight-binding model, we find that the integral of the frequency-dependent shift-current tensor is well correlated to the spontaneous polarization; and this integral is maximized at an optimal value of polarization.

*Structure, symmetries, and ab-initio methods.*— Our DFT calculations are performed with the generalized gradient approximation including spin-orbit coupling. We use the ABINIT code [20], with Gaussian pseudopotentials [21] and the Perdew-Burke-Ernzerhof (PBE) functional [22]. We fully relax atomic positions in supercells

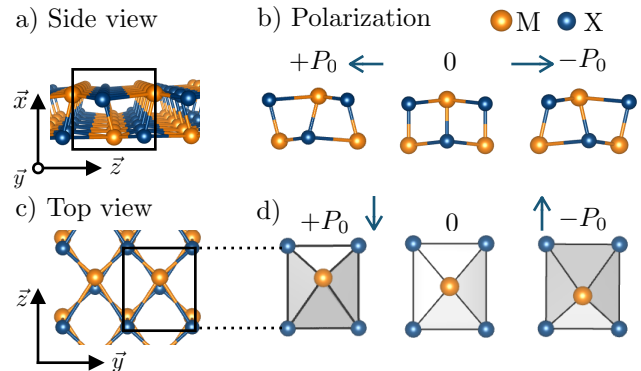


FIG. 1. (Color online) The crystal structure of single-layer group-IV monochalcogenides  $MX$ , where  $M=\text{Ge, Sn}$ , and  $X=\text{S, Se}$ . In (a) we show the 3D view of the single-layer and in (b)-(d) the projections of the single layer crystal on the Cartesian axes. Structures with  $0, \pm P_0$  polarizations are also shown in inset (b) and (d). A twofold rotation along  $z$  (plus translations) determines the polarization axis, see text.

TABLE I. Left: Ground state polarization of single-layer monochalcogenides. The 3D effective polarizations are for a layer thickness of  $a = 2.6$  Å. The energy barrier between the ground-states with opposite polarization calculated within DFT-PBE are also shown. Right: Direct (D) and indirect (I) band gaps calculated with DFT-PBE and optical gaps reported from *GW*-BSE calculations.

	Polarization		Energy barrier (K)	Supercell lattice vectors (Å)			DFT-PBE		Band gap (eV)		Expt. <sup>a</sup> D
	2D (nC/m)	3D (C/m <sup>2</sup> )		$a$	$b$	$c$	D	I	D	<i>GW</i> -BSE	
GeS	0.48	1.9	5563	15.0	3.7	4.5	1.9	1.7	2.2 [19]	1.6 [12]	
GeSe	0.34	1.3	1180	15.0	4.0	4.3	1.2	1.2	1.6, 1.3 [18, 19]	1.2 [12]	
SnS	0.24	0.8	384	15.0	4.1	4.3	1.5	1.4			
SnSe	0.17	0.6	80	15.0	4.3	4.4	0.9	0.9	1.4 [18]		

<sup>a</sup> Experimental optical gaps (Expt.) of few-layer chalcogenides are also shown for comparison.

that include at least 10 Å of vacuum between layers. Our relaxed lattice parameters are shown in Table I and agree with previous work [10] (see details in Supplementary Material [23], which includes Ref. [24]).

Bulk monochalcogenide crystals  $MX$  ( $M=\text{Ge, Sn}$  and  $X=\text{S, Se}$ ) are orthorhombic with point group  $mmm$  and space group  $Pnma$  (No. 62). They consist of van der Waals-bonded double layers of metal monochalcogenide atoms in an armchair arrangement. The space group of the bulk crystal contains eight symmetries including a center of inversion which prevents spontaneous electric polarization and the BPVE. Upon exfoliation, the resulting single “double layer” primitive cell has four atoms. In this work, the layers are chosen to be oriented perpendicular to the  $x$  axis as shown in Fig. 1(a). The single-layer structure has four symmetries, including a two-fold rotation with respect to  $z$  (plus translation),  $2[001] + (1/2, 0, 1/2)$ , which determines the direction of the in-plane spontaneous polarization of the layer along the  $z$  axis. In addition, the 2D system has two mirror symmetries with respect to  $x$  and  $y$ ,  $m[100] + (1/2, 1/2, 1/2)$  and  $m[010] + (0, 1/2, 0)$ . Hence its point group, which determines the nonzero components of the optical response tensors, is  $mm2$ .

As a consequence of the mirror symmetries with respect to the  $x$  and  $y$  axis of a single monochalcogenide layer, all the cross-components terms of the imaginary part of the dielectric function,  $\epsilon_2^{ab}$ , vanish together with the tensor components  $xxx$ ,  $xyy$ ,  $xzz$ ,  $yxx$ ,  $yyy$ , and  $yzz$  of the shift current. Only seven components are symmetry allowed [25]:  $zxx$ ,  $zyy$ ,  $zzz$ ,  $yyz$ , and  $xzx$ , as well as components obtained by interchanging the last two indices. Symmetry, however, does not dictate the magnitude of the response in each direction, and consequently we compute the matrix elements below.

*Spontaneous polarization.*— We calculate the spontaneous polarization of single-layer chalcogenides using the modern theory of polarization [26, 27], as implemented in ABINIT. We first identify an adiabatic path between the ground state and a centrosymmetric geometry with, in

this case, zero polarization. We parametrize the atomic displacements along a path between these geometries [Figs. 1(b) and 1(d)] with  $\lambda$  as  $\mathbf{R}^i(\lambda) = \mathbf{R}_0^i + \lambda(\mathbf{R}_f^i - \mathbf{R}_0^i)$ , where  $\mathbf{R}_0^i$  ( $\mathbf{R}_f^i$ ) is the initial (final) position of  $i$ th atom in the centrosymmetric (noncentrosymmetric) structure. We calculate the minimum-energy path between the  $\pm P_0$  configurations, as detailed in the Supplementary Material [23]. The minimal energy path is indistinguishable from the linear path used here. The polarization for various 2D monochalcogenides has also been theoretically studied recently [13, 17, 28–33]. Our adiabatic polarization path, is shown schematically in Figs. 1(b) and Figs. 1(d). Table I shows the computed spontaneous electric polarization per unit area,  $P_0a$ , and an effective 3D polarization assuming an active single-layer thickness  $a = 2.6$  Å. Interestingly, GeSe has a significantly higher effective 3D polarization, 1.9 C/m<sup>2</sup>, than most prototypical ferroelectrics, e.g., 0.0028 C/m<sup>2</sup> in CaMn<sub>7</sub>O<sub>12</sub> [34], 0.26 C/m<sup>2</sup> in BaTiO<sub>3</sub> [35, 36], 0.37 C/m<sup>2</sup> in KNbO<sub>3</sub> [37] and 0.9 C/m<sup>2</sup> in BiFeO<sub>3</sub> [38, 39]. The energy barriers, provided in Table I, are much larger than room temperature. However, since reorientation under an applied electric field is often facilitated by domain wall motion, future experiments are necessary to conclusively demonstrate ferroelectric switching behavior.

*Optical absorption and shift current.*— One notable feature of single-layer monochalcogenides is their promising band gap energies in the visible range [12, 18, 19]. In Table I, we show the computed DFT-PBE gaps, which are a good estimate of the corresponding optical gaps. Although in principle *ab initio* many-body perturbation theory (MBPT) would be a more rigorous approach to optical gaps, in this case, we expect the PBE single-particle gaps to be indicative since excitonic effects, as large as 1 eV in GeS [19], can fortuitously cancel the well-known tendency of the PBE functional to underestimate the transport gap. In Sn-based materials, the PBE gaps are smaller by  $\sim 0.5$  eV than in prior MBPT calculations (see Table I), and hence the responses are redshifted and should be treated with more caution. In addition, since

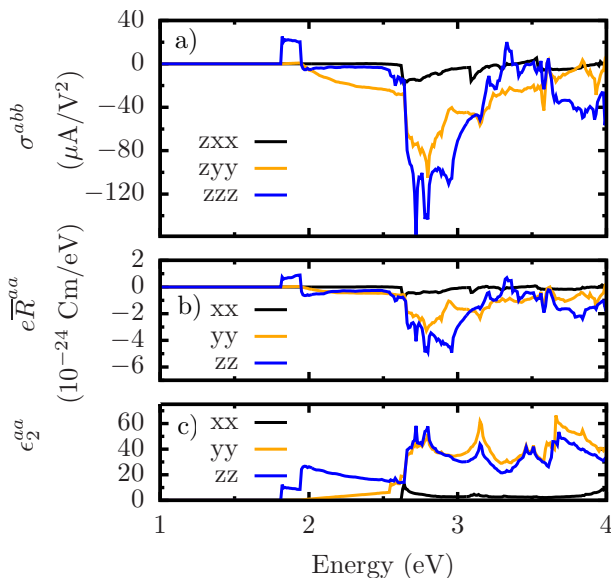


FIG. 2. (Color online) Shift-current spectra (a), shift vector integrated over  $\mathbf{k}$  (b), and linear absorption (c) of single-layer GeS. The large in-plane shift-current response in the visible range is dominated by the shift vector and corresponds to the large absorption along  $zz$  and  $yy$ .

exciton formation can alter and even enhance shift current at exciton resonances [40], strong excitonic effects in monochalcogenides could lead to even larger shift currents.

We calculate the imaginary part of the dielectric function,  $\epsilon_2^{ab}$ , within the independent particle approximation. As shown in Fig. 2, the absorption is strong  $\epsilon_2 \sim 50$ , in the visible range of 1.5 to 3 eV, due to the direct or nearly direct band gap of these materials [7]. For comparison, we calculate the absorption coefficient  $\alpha = \omega\epsilon_2/c$ , with light frequency  $\omega$  and speed of light  $c$ . For the 2D monochalcogenides of thickness  $\sim 2.6$  Å,  $\alpha \sim 0.5\text{--}1.5 \times 10^6 \text{cm}^{-1}$ , and similar values were found for graphene and MoS<sub>2</sub> ( $0.7$  and  $1\text{--}1.5 \times 10^6 \text{cm}^{-1}$ , respectively) [41]. The  $zz$  and  $yy$  tensor components are larger than  $xx$  due to the intrinsic crystal anisotropy, in agreement with previous work [12, 18, 19]. In addition to the energy gaps and the large absorption in the visible range, single-layer monochalcogenides have a large shift-current response, as shown below.

The dc shift current is generated to second order in the electric field. Consider a monochromatic electric field of the form  $E^b(t) = E^b(\omega)e^{i\omega t} + E^b(-\omega)e^{-i\omega t}$ . The shift-current response can be expressed in terms of the third-rank tensor  $\sigma^{abc}(0; \omega, -\omega)$  as,

$$J_{\text{shift}}^a(\omega) = 2 \sum_{bc} \sigma^{abc}(0; \omega, -\omega) E^b(\omega) E^c(-\omega). \quad (1)$$

The shift-current tensor is given by [3]

$$\sigma^{abc}(0; \omega, -\omega) = -\frac{i\pi e^3}{2\hbar^2} \int \frac{d\mathbf{k}}{8\pi^3} \sum_{nm} f_{nm} (r_{mn}^b r_{nm}^c{}_{;a} + r_{mn}^c r_{nm}^b{}_{;a}) \delta(\omega_{mn} - \omega), \quad (2)$$

where  $r_{mn}^a$  are velocity matrix elements. The  $r_{mn}^a{}_{;b}$  are generalized derivatives, defined as  $r_{mn}^a{}_{;b} = \partial r_{mn}^a / \partial k^b - i(A_{nn}^b - A_{mm}^b) r_{nm}^a$ , where  $A_{nm}^a$  are the Berry connections, with the  $a$  and  $b$  indices denoting Cartesian directions. We define the Fermi-Dirac occupation numbers  $f_{nm} = f_n - f_m$ , and the band energy differences as  $\hbar\omega_{nm} = \hbar\omega_n - \hbar\omega_m$ . For linearly polarized incident light,  $b = c$ , and the integrand in Eq. (2) is proportional to the shift “vector”  $R_{nm}^{ab}$  [3], defined as  $(1/2)\text{Im}[r_{nm}^b r_{mn}^b{}_{;a} - r_{mn}^b r_{nm}^b{}_{;a}] |r_{nm}^b|^{-2}$ .

Figure 2 shows the calculated effective shift-current spectra for GeS parallel and perpendicular to the polarization axis. (The shift-current spectra for GeSe, SnS, and SnSe have similar features, see Supplementary Material [23].) We report the responses assuming an active single-layer thickness of  $a = 2.6$  Å [42]. We find a broad maximum of the order of  $100 \mu\text{A}/\text{V}^2$  which, importantly, occurs in the visible range ( $1.5\text{--}3.3$  eV). The in-plane components,  $zzz$  and  $zyy$ , are larger than the out-of-plane component  $zxx$ , consistent with the large absorption along  $zz$  and  $yy$ . We compare this response with that of prototypical ferroelectric materials in the same frequency range, e.g.,  $0.05 \mu\text{A}/\text{V}^2$  in BiFeO<sub>3</sub> [5], and  $5 \mu\text{A}/\text{V}^2$  in BaTiO<sub>3</sub> [5], which are much smaller. Additionally,  $0.5 \mu\text{A}/\text{V}^2$  is reported for hybrid halide perovskites [5] and NaAsSe<sub>2</sub> [44], and  $250 \mu\text{A}/\text{V}^2$  ( $= 400 \text{mA}/\text{W}$ ) is found for state-of-the-art Si-based solar cells [45] (see the Supplementary Material [23] for details on the conversion between shift-current and A/W units). The BPVE for 2D monochalcogenides is therefore quite large.

The absorption and shift-current spectra are related by the velocity matrix elements  $r_{nm}$  entering Eq. (2), explaining why peaks in  $\epsilon_2$  tend to correspond to peaks in the shift current spectra. To explore the relationship between  $\epsilon_2^{bb}$  and  $\sigma^{abb}$ , in Fig. 2(b), we plot the shift vector integrated over the Brillouin zone (BZ) [5, 46],

$$e\bar{R}^{ab}(\omega) = e\Omega \int \frac{d\mathbf{k}}{8\pi^3} \sum_{nm} f_{nm} R_{nm}^{ab} \delta(\omega_{nm} - \omega), \quad (3)$$

where  $\Omega$  is the volume of the unit cell. For the monochalcogenides,  $e\bar{R}^{bb}(\omega)$  contains most features of  $\sigma^{abb}(\omega)$ , and hence dominates the shift-current response. Following the analysis of Ref. [46], we interpret  $e\bar{R}^{ab}$  as a collective shift of polarization upon excitation, due to transitions from valence to conduction states with a distinct center of mass [47]. Thus, wave function Berry phases play a fundamental role in the BPVE, which we further explore next.

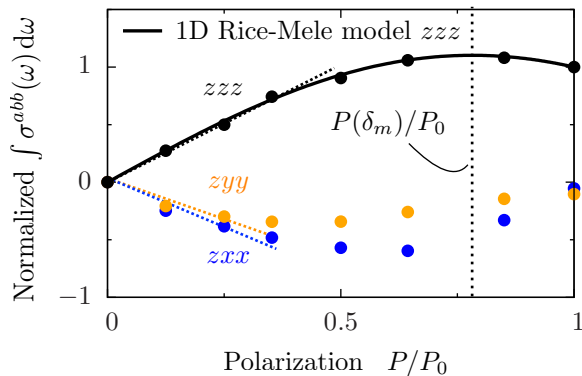


FIG. 3. (Color online) Nonmonotonic dependence of the integral of the shift-current tensor vs electric polarization for GeS; the integral is normalized by  $-3 \times 10^{10} \text{ As}^{-1}\text{V}^{-2}$ , its value at the ground state with polarization  $P_0 = 1.9 \text{ C/m}^2$ . The tensor components  $zzz$ ,  $zyy$ , and  $zxx$  are shown in black, green, and blue points, respectively. For small  $P$  the integral is directly proportional to polarization (dashed lines), but it is nonmonotonic for large  $P$ . The integral reaches its maxima at  $P(\delta_m)$ , which is close to  $P_0$ .

*Polarization and shift current.*— To understand the relation between  $\sigma^{abb}$  and polarization  $P$ , consider a short-circuit bulk ferroelectric illuminated by unpolarized light with a flat broad spectrum. The short-circuit current in the  $z$  direction,  $I_{sc} = AE_0^2 \int d\omega (\sigma^{zyy}(0; \omega, -\omega) + \sigma^{zzz}(0; \omega, -\omega))$ , is proportional to the integral of the shift current tensor. Here, the cross sectional area is  $A$  and the amplitude of the electric field is  $E_0$ . To first nonvanishing order in  $\lambda$ , both the polarization and the integral are linear in  $\lambda$ ,  $P(\lambda) = \partial_\lambda P(0) \lambda + \dots$ ,  $\int \sigma^{abb}(\lambda) = (\int \partial_\lambda \sigma^{abb}(0)) \lambda + \dots$ , and hence proportional to each other.

In Fig. 3 we show the integral of the shift-current tensor over the frequency range (up to 6 eV) for GeS as a function of polarization along the adiabatic path of Fig. 1(b). For small polarization, the integral grows linearly with polarization, as expected. However, for larger polarization there is nonmonotonic behavior which we explain below with a tight-binding model. Notice that without the integral, the expansion coefficients become frequency dependent and the current could increase or decrease with polarization with no general relationship.

*The Rice-Mele tight-binding model.*— As mentioned previously, the monochalcogenide layer has a  $2[001] + (1/2, 0, 1/2)$  symmetry that transforms the upper three atoms in Fig. 1(b) onto the lower three. This suggests there is an effective one-dimensional description of the armchair structure in the  $z$  direction, and in fact, as we show below, the trends in the integral of the shift-current tensor along  $z$  are captured by a simple model Rice-Mele

(RM) model [48, 49]. The RM Hamiltonian is

$$H = \sum_i \left[ \left( \frac{t}{2} + (-1)^i \frac{\delta}{2} \right) (c_i^\dagger c_{i+1} + h.c.) + (-1)^i \Delta c_i^\dagger c_i \right], \quad (4)$$

where  $\delta$  parametrizes the structural distortion relative to the centrosymmetric structure,  $\Delta$  the staggered on-site potential, and  $c_i^\dagger$  is the creation operator for electrons at site  $i$ . Inversion symmetry is broken when both  $\Delta \neq 0$  and  $\delta \neq 0$ , and preserved otherwise. For this two-band model Eq. (2) gives (see Supplementary Material [23] for more details),

$$\int d\omega \sigma^{zzz}(0; \omega, -\omega) = e^3 \int dk \frac{|v_{cv}|^2 R_{cv}}{4E^2}, \quad (5)$$

where  $R_{cv} = \partial \phi_{cv} / \partial k + A_{cc} - A_{vv}$  is the shift vector and is gauge invariant.  $A_{nm} = i \langle u_n | \partial_k | u_m \rangle$  are the Berry connections, and  $\phi_{nm}^b$  is defined by  $r_{nm}^b = |r_{nm}^b| e^{-i\phi_{nm}^b}$ , where  $E(k)$  is the band dispersion and  $v_{cv}$  is the matrix element of the velocity operator. The Rice-Mele model allows for a complete analytic solution for the optical response and these results will be presented elsewhere [50]. The polarization is  $P(\delta) = (e/2\pi) \int dk [A_{vv}(k, \delta) - A_{vv}(k, 0)]$ . The model has two independent parameters  $\delta$  and  $\Delta$ . To make contact with the monochalcogenides, we set  $t = 1$ , and  $\delta$  and  $\Delta$  are related by the energy gap,  $2\sqrt{\delta_0^2 + \Delta_0^2} = 1.9 \text{ eV}$  (for GeS). Choosing parameters  $(t, [0, \delta_0], \Delta_0) = (1, [0, -0.87], 0.4) \text{ eV}$  fits the  $zzz$  *ab initio* integral for GeS well and corresponds to a gap of 1.9 eV. The RM model polarization is  $P_0 = P(\delta_0)$ .

As the RM model is a good description of the integral of the shift-current tensor in monochalcogenides, we now explore the relation between polarization and shift current within this model. The integral of the shift current tensor in Eq. (5) is determined by the competition between the shift vector and the velocity matrix elements  $\hbar^2 |v_{cv}|^2 / 4E^2 \equiv |r_{cv}|^2$ . These in turn are controlled by  $\delta$  and  $\Delta$ , which have opposing tendencies: whereas increasing  $\Delta$  tends to localize charge at lattice sites, increasing dimerization  $\delta$  moves the center of charge away from them (leading to an increase in polarization). We find that for  $\delta \ll \Delta$ ,  $R_{cv}$  is sharply peaked at  $k = 0$  but  $|v_{cv}|^2 / 4E^2$  peaks at  $\pi/c$ , and hence the integral is small. As  $\delta$  increases,  $R_{cv}$  and  $|v_{cv}|^2 / 4E^2$  broaden, and the integral increases; the integral reaches a maximum at an optimum value,  $\pm \delta_m$  which to lowest order in  $\Delta$  is

$$\delta_m = \Delta + O(\Delta^3 \log \Delta), \quad (6)$$

where the polarization takes the value  $P(\delta_m)$ . For GeS, GeSe, and SnS,  $\delta_0$  ( $-0.9$ ,  $-0.5$ , and  $-0.6$  respectively) is relatively close to the optimal  $\delta_m$  values of  $-0.5$ ,  $-0.5$ , and  $-0.6$ , respectively, whereas for SnSe  $\delta_m$  ( $0.4$ ) is farthest from  $\delta_0$  ( $-0.2$ ), see the Supplementary Material [23]. Therefore, consistent with Refs. 7 and 5, the large

shift current in these monochalcogenides results from two competing factors, a large shift vector and large velocity matrix elements (linear absorption strength), both of which can be modulated with polarization (and therefore composition, structure, and external electric field).

*Discussion and conclusions.*— We have calculated the shift-current response and spontaneous electric polarization of a family single-layer monochalcogenides, MX, where  $M=Ge, Sn$ , and  $X=S, Se$ . We find a large shift current and a large polarization compared with prototypical ferroelectric materials. The fact that the maximum current occurs in the visible range highlights the potential of these materials for optoelectronic applications. Further, the large spontaneous polarization can serve as a knob to engineer the photoresponse. The integral of the shift-current tensor over frequency is clearly dependent on polarization and by means of a RM model, we find an optimal value of polarization where the current is maximum.

We thank J. Sipe, F. de Juan, S. Barraza-Lopez, S. Coh, R. A. Muniz, and S. E. Reyes-Lillo for useful discussions. This work is supported by the U.S. Department of Energy, Director, Office of Science, Office of Basic Energy Sciences, Materials Sciences and Engineering Division, under Contract No. DE-AC02-05CH11231, through the Theory FWP (KC2301) at Lawrence Berkeley National Laboratory (LBNL). B.M.F. acknowledges support from AFOSR MURI, Conacyt, and NERSC Contract No. DE-AC02-05CH11231. This work is also supported by the Molecular Foundry through the DOE, Office of Basic Energy Sciences under the same contract number. T.M. acknowledges support from the Gordon and Betty Moore Foundation's EPiQS Initiative Theory Center Grant. J.E.M. acknowledges Laboratory Directed Research and Development funding from LBNL Contract No. DEAC02-05CH11231. B.S.M. acknowledges partial support from CONACYT-Mexico GoGa No. 153930. We acknowledge the use of computational resources at the NERSC.

B.M.F. and T.R. contributed equally to this work.

---

\* These two authors contributed equally.

- [1] B. I. Sturman and P. J. Sturman, *Photovoltaic and Photo-refractive Effects in Noncentrosymmetric Materials* (CRC Press, Boca Raton, Florida, 1992).
- [2] R. von Baltz and W. Kraut, Phys. Rev. B **23**, 5590 (1981).
- [3] J. E. Sipe and A. I. Shkrebtii, Phys. Rev. B **61**, 5337 (2000).
- [4] L. Z. Tan, F. Zheng, S. M. Young, F. Wang, S. Liu, and A. M. Rappe, NPJ Comput. Mater. **2**, 16026 (2016).
- [5] S. M. Young, F. Zheng, and A. M. Rappe, Phys. Rev. Lett. **109**, 236601 (2012); S. M. Young and A. M. Rappe, *ibid.* **109**, 116601 (2012); F. Zheng, H. Takenaka, F. Wang, N. Z. Koocher, and A. M. Rappe, J. Phys. Chem. Lett. **6**, 31 (2015); S. M. Young, F. Zheng, and A. M. Rappe, Phys. Rev. Appl. **4**, 054004 (2015).
- [6] A. Zenkevich, Y. Matveyev, K. Maksimova, R. Gaynutdinov, A. Tolstikhina, and V. Fridkin, Phys. Rev. B **90**, 161409 (2014).
- [7] A. M. Cook, B. M. Fregoso, F. de Juan, and J. E. Moore, Nat. Commun. **8**, 14176 (2017).
- [8] Y. B. Lyanda-Geller, S. Li, and A. V. Andreev, Phys. Rev. B **92**, 241406 (2015).
- [9] L. Li, Z. Chen, Y. Hu, X. Wang, T. Zhang, W. Chen, and Q. Wang, J. Am. Chem. Soc. **135**, 1213 (2013).
- [10] A. K. Singh and R. G. Hennig, Appl. Phys. Lett. **105**, 042103 (2014).
- [11] F. Wang, S. M. Young, F. Zheng, I. Grinberg, and A. M. Rappe, Nat. Commun. **7**, 10419 (2016).
- [12] P. Ramasamy, D. Kwak, D.-H. Lim, H.-S. Ra, and J.-S. Lee, J. Mater. Chem. C **4**, 479 (2016).
- [13] M. Wu and X. C. Zeng, Nano Lett. **16**, 3236 (2016).
- [14] C. Kamal, A. Chakrabarti, and M. Ezawa, Phys. Rev. B **93**, 125428 (2016).
- [15] S.-D. Guo and Y.-H. Wang, Journal of Applied Physics **121**, 034302 (2017).
- [16] C. Xin, J. Zheng, Y. Su, S. Li, B. Zhang, Y. Feng, and F. Pan, J. Phys. Chem. C **120**, 22663 (2016).
- [17] P. Z. Hanakata, A. Carvalho, D. K. Campbell, and H. S. Park, Phys. Rev. B **94**, 035304 (2016).
- [18] G. Shi and E. Kioupakis, Nano Lett. **15**, 6926 (2015).
- [19] L. C. Gomes, P. E. Trevisanutto, A. Carvalho, A. S. Rodin, and A. H. Castro Neto, Phys. Rev. B **94**, 155428 (2016).
- [20] X. Gonze *et al.*, Comput. Phys. Commun. **205**, 106 (2016).
- [21] M. Krack, Theor. Chem. Acc. **114**, 145 (2005).
- [22] J. P. Perdew, K. Burke, and M. Ernzerhof, Phys. Rev. Lett. **77**, 3865 (1996).
- [23] See Supplemental Material at <http://link.aps.org/supplemental/10.1103/PhysRevLett.119.067402> for details on numerical calculations of shift current spectra for GeSe, GeS, SnS and SnSe.
- [24] F. Nastos, J. Rioux, M. Strimas-Mackey, B. S. Mendoza, and J. E. Sipe, Phys. Rev. B **76**, 205113 (2007).
- [25] P. N. Butcher, *Nonlinear Optical Phenomena* (Engineering Experiment Station of the Ohio State University, Columbus OH., 1965).
- [26] D. Vanderbilt and R. D. King-Smith, Phys. Rev. B **48**, 4442 (1993).
- [27] R. Resta, J. Phys.: Condens. Matter **22**, 123201 (2010).
- [28] L. C. Gomes, A. Carvalho, and A. H. Castro Neto, Phys. Rev. B **92**, 214103 (2015).
- [29] R. Fei, W. Li, J. Li, and L. Yang, Appl. Phys. Lett. **107**, 173104 (2015).
- [30] M. Mehboudi, B. M. Fregoso, Y. Yang, W. Zhu, A. van der Zande, J. Ferrer, L. Bellaiche, P. Kumar, and S. Barraza-Lopez, Phys. Rev. Lett. **117**, 246802 (2016).
- [31] R. Fei, W. Kang, and L. Yang, Phys. Rev. Lett. **117**, 097601 (2016).
- [32] M. Mehboudi, A. M. Dorio, W. Zhu, A. van der Zande, H. O. H. Churchill, A. A. Pacheco-Sanjuan, E. O. Harriss, P. Kumar, and S. Barraza-Lopez, Nano Lett. **16**, 1704 (2016).
- [33] H. Wang and X. Qian, 2D Mater. **4**, 015042 (2017).
- [34] R. D. Johnson, L. C. Chapon, D. D. Khalyavin, P. Manuel, P. G. Radaelli, and C. Martin, Phys. Rev. Lett. **108**, 067201 (2012).



- [35] A. von Hippel, *Rev. Mod. Phys.* **22**, 221 (1950).  
 [36] J. Shieh, J. Yeh, Y. Shu, and J. Yen, *Mater. Sci. Eng.: B* **161**, 50 (2009).  
 [37] R. Resta, M. Posternak, and A. Baldereschi, *Phys. Rev. Lett.* **70**, 1010 (1993).  
 [38] J. B. Neaton, C. Ederer, U. V. Waghmare, N. A. Spaldin, and K. M. Rabe, *Phys. Rev. B* **71**, 014113 (2005).  
 [39] G. Catalan and J. F. Scott, *Adv. Mater.* **21**, 2463 (2009).  
 [40] T. Morimoto and N. Nagaosa, *Phys. Rev. B* **94**, 035117 (2016).  
 [41] M. Bernardi, M. Palummo, and J. C. Grossman, *Nano Lett.* **13**, 3664 (2013).  
 [42] Here we show that a single-layer monochalcogenide has a large shift current response, moreover, in the Supplementary Material [23] we show that the response of a thick 3D array of slabs, characterized by the Glass coefficient [43], is also large.  
 [43] A. M. Glass, D. von der Linde, and T. J. Negran, *Appl. Phys. Lett.* **25**, 233 (1974).  
 [44] J. A. Brehm, S. M. Young, F. Zheng, and A. M. Rappe, *J. Chem. Phys.* **141**, 204704 (2014).  
 [45] M. Pagliaro, G. Palmisano, and R. Ciriminna, *Flexible Solar Cells* (Wiley-VCH, Weinheim, 2008).  
 [46] B. M. Fregoso, T. Morimoto, and J. E. Moore, *Phys. Rev. B* **96**, 075421 (2017).  
 [47] The integral of the shift vector over  $\mathbf{k}$ ,  $\bar{R}$  has been studied for complex ferroelectric materials, such as  $\text{BiTiO}_3$  and  $\text{PbTiO}_3$  in Ref. 5.  
 [48] D. Vanderbilt and R. D. King-Smith, *Phys. Rev. B* **48**, 4442 (1993).  
 [49] S. Onoda, S. Murakami, and N. Nagaosa, *Phys. Rev. Lett.* **93**, 167602 (2004).  
 [50] B. M. Fregoso *et al.*, (to be published).  
 [51] The ABINIT web site: <http://www.abinit.org>.  
 [52] The Tiniba web site: <https://github.com/bemese/tiniba>.

### Supplementary information: Large bulk photovoltaic effect and spontaneous polarization of single-layer monochalcogenides

In this Supplementary Information we present details of our electric polarization and shift current calculation for GeS, GeSe, SnS and SnSe. We also provide details of the shift current and polarization in the Rice-Mele model.

#### Numerical details

Our density functional theory (DFT) calculations are done with the ABINIT code [20] and within the Perdew-Burke-Ernzerhof functional (PBE) [22]. We use Hartwigsen-Goedecker-Hutter norm conserving pseudopotentials available in the ABINIT web site [51]. We use an energy cut-off of 40 hartrees to expand the plane-wave basis set. To model the slabs we use supercells with 15 Å along the non-periodic direction, which corresponds to  $> 10$  Å of vacuum. To calculate  $\sigma$  we include 20 valence and 30 conduction bands, which accounts for all allowed transitions in the low energy range;

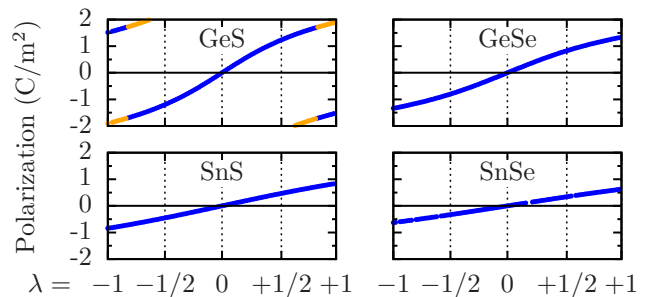


FIG. 4. Polarization along adiabatic path parametrized by  $\lambda$ . The gap does not close along the path and takes the system from polarization  $-P_0$  ( $\lambda = -1$ ) to 0 ( $\lambda = 0$ ) to  $+P_0$  ( $\lambda = +1$ ). The calculated polarization (blue dots) is shifted by the twice polarization quantum ( $Q = 1.7 \text{ C/m}^2$ ) for GeS (orange dots).

up to 6 eV; we use a mesh of  $70 \times 70$  k-points along the periodic slab directions and integrate using a tetrahedron method. Worth mentioning that the optical-response and spontaneous-polarization magnitude depend on the calculation volume, therefore we renormalize our results to the atomic slab widths (removing the vacuum) of 2.56, 2.61, 2.84 and 2.73 Å for GeS, GeSe, SnS and SnSe respectively. String method calculations were done with the ABINIT code as explained in Sect. 3.2 of Ref. 20, where the minimal energy path between two points was found using 50 images and a tolerance on the mean total energy for images of  $2 \times 10^{-6}$  hartrees. In the next, we provide more details on our calculations of spontaneous polarization, the ferroelectric energy barrier and optical responses of the monochalcogenides.

#### Spontaneous Polarization

We calculate the spontaneous polarization as implemented in ABINIT using

$$P^a(\lambda) = \sum_i \frac{eZ^i r_i^a(\lambda)}{\Omega} - ie \sum_v \int_{\text{BZ}} \frac{d\mathbf{k}}{(2\pi)^3} \langle u_v^\lambda | \nabla^a u_v^\lambda \rangle, \quad (7)$$

where  $u_v^\lambda$  are Bloch wave functions,  $Z^i$  is the atomic number of the  $i$ th atom,  $\Omega$  is the simulation volume.  $\lambda$  parametrizes an adiabatic path from a centrosymmetric configuration to the ground-state configuration. The polarization is defined as the difference between the polarization of two smoothly connected atomic structures:  $\mathbf{R}_0^i$  with inversion symmetry (i.e., zero of polarization) and  $\mathbf{R}_f^i(\lambda = 1)$ , where  $\mathbf{R}_f^i = \mathbf{R}_0^i + \lambda(\mathbf{R}_f^i - \mathbf{R}_0^i)$ . The geometry of the  $\mathbf{R}_f^i$  and  $\mathbf{R}_0^i$  points used in this work are shown in Table III. The polarization calculated at small steps of  $\lambda$  for the different crystals is shown in Fig. 4. Since all points are connected smoothly, the polarization is well-defined and can be calculated as the difference

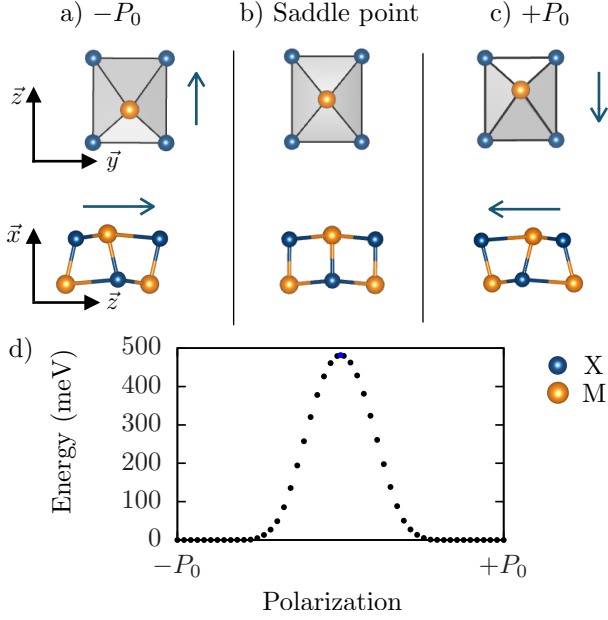


FIG. 5. Ferroelectric energy barrier of GeS calculated using the string method. Insets a-c: ground state configurations with polarization  $\pm P_0$  and saddle point. Inset d shows the calculated energy barrier, with the saddle point in blue.

between the polarization at  $\mathbf{R}_0^i$  and  $\mathbf{R}_f^i$ . The resulting spontaneous polarization values of the different crystals are tabulated in Table. 1 of the main manuscript.

### Minimum energy path

Here we detail how we evaluate the ferroelectric energy barrier between the two ground-states with inverse polarization  $\pm P_0$ . Here we assume the NVT ensemble, i.e. we keep the cell-dimensions constant. We first calculate a path of fifty equidistant-potential points connecting the two frontier points using the string method. Note that with this grid of points we cannot evaluate the polarity of the central point due to numerical remaining errors. Hence, to obtain the precise coordinates of the saddle point, for GeS we calculate a finer grid of thirty equidistant-potential points in between the two central points of the fifty-point initial path. In Fig. 5 we show the energy barrier and initial, central and final configurations along the trajectory for GeS. The resulting coordinates of the highest-energy saddle point (Fig. 5b) are

Atom coordinates ( $\text{\AA}$ ):

Ge	1.54	0.91	0.00
Ge	3.84	2.74	2.24
S	3.86	0.91	0.00
S	1.51	2.74	2.24

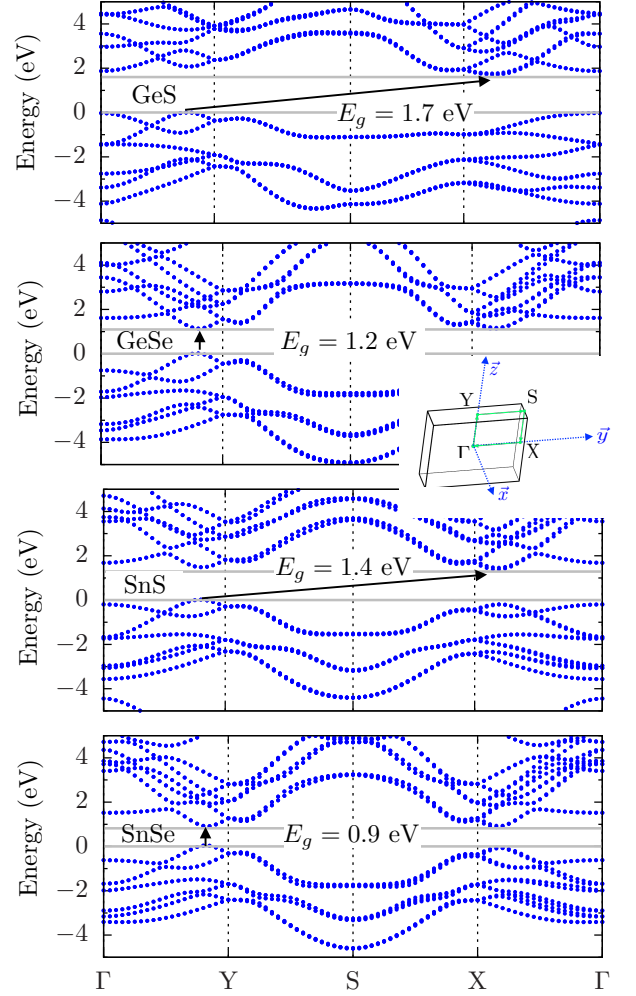


FIG. 6. Electronic bandstructure of group-IV single-layer monochalcogenides, calculated within DFT-PBE. We choose a k-point path along the Brillouin zone, shown at the bottom.

which resemble those of the ideal  $R_0$  point (see Fig.1 of the main text and coordinates in Table III); while the  $x$  Cartesian component is slightly modified by  $\sim 0.1$  bohr, the  $y$  and  $z$  Cartesian components are identical, implying zero-polarization along  $z$ . In terms of energetics, the saddle-point total energy is  $\sim 70$  meV lower than that of the  $R_0$  point.

### Electronic bandstructures

The electronic bandstructures calculated within DFT are shown in Fig. 6, these agree with previous works [10]. For each material the fundamental gap  $E_g$  is indicated in the figure with an arrow.

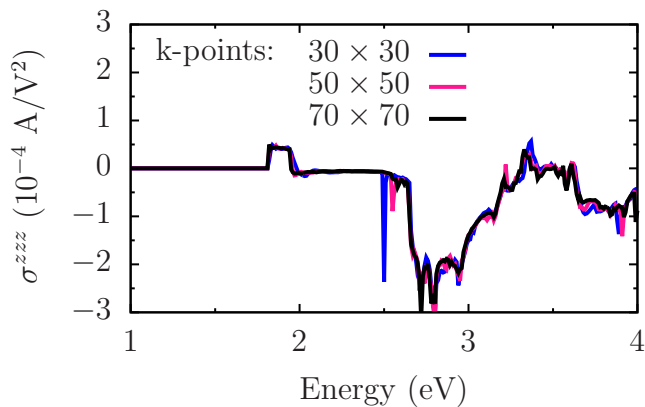


FIG. 7. Convergence of shift-current tensor for GeS with respect to the  $\mathbf{k}$ -mesh size.

### Linear and shift-current spectra

We calculate the linear absorption within the independent-particle approximation,

$$\epsilon_2^{ab}(\omega) = \delta_{ab} - \frac{e^2\pi}{\epsilon_0\hbar} \int \frac{d\mathbf{k}}{(2\pi)^3} \sum_{nm} f_{nm} r_{nm}^a r_{mn}^b \delta(\omega_{mn} - \omega), \quad (8)$$

which provides a RPA frequency dependent optical absorption spectrum. Here  $r_{nm}^a = A_{nm}^a = i\langle u_n | \nabla^a | u_m \rangle$  ( $n \neq m$ ) are the velocity matrix elements and  $A_{nm}^a$  the usual Berry connections, with the  $a$  and  $b$  indices indicating one of the three Cartesian directions. We define the occupations numbers  $f_{nm} = f_n - f_m$ , and the band energy differences as  $\hbar\omega_{nm} = \hbar\omega_n - \hbar\omega_m$ . Here and in what follows we assume zero temperature.

The shift-current response is calculated from Eq. (2) of the manuscript,

$$\sigma^{abc}(0; \omega, -\omega) = -\frac{i\pi e^3}{2\hbar^2} \int \frac{d\mathbf{k}}{8\pi^3} \sum_{nm} f_{nm} (r_{mn}^b r_{nm;a}^c + r_{mn}^c r_{nm;a}^b) \delta(\omega_{mn} - \omega). \quad (9)$$

First, we calculate the wavefunctions  $\psi_m$  and eigenvalues using ABINIT. The velocity matrix elements are computed with a plane-wave expansion,

$$\psi_n(\mathbf{k}; \mathbf{r}) = \sum_{\mathbf{G}} C_{m\mathbf{k}}(\mathbf{G}) e^{i(\mathbf{k}+\mathbf{G})\cdot\mathbf{r}}, \quad (10)$$

such as,

$$r_{mn}(\mathbf{k}) = \hbar \sum_{\mathbf{G}} C_{m\mathbf{k}}^*(\mathbf{G}) C_{n\mathbf{k}}(\mathbf{G}) (\mathbf{k} + \mathbf{G}) \quad (11)$$

where  $C_{m\mathbf{k}}(\mathbf{G})$  are expansion coefficients of the plane-wave  $\mathbf{G}$  vectors. Subsequently, the generalized derivatives  $r_{nm;b}$  are calculated from velocity matrix elements

as in Ref. [3] (see Section VIII). We accelerate convergence on  $\mathbf{k}$  points by using a tetrahedron-integration method [24]. The optical responses are calculated with the Tiniba code, see further details in Ref. 52.

We noticed that shift-current response converges relatively slow with respect to the number of  $\mathbf{k}$ -points. As shown in Fig. 7, for GeS we require a dense mesh of  $70 \times 70$   $\mathbf{k}$ -points on the slab plane to converge, removing sudden jumps (e.g., see blue and pink lines close 2.5 eV) in the response.

In Fig. 8, we show our calculated linear and shift-current responses of the layered monochalcogenide materials studied in this work. As mentioned in the main text, the responses are related by the matrix elements  $|r_{nm}|^2$  entering in Eqs. 8 and 9. Therefore, peaks in  $\epsilon_2$  tend to correspond to peaks in  $\sigma$ , and the shift-current responses along  $zzz$  and  $zyy$  are larger than for  $zxx$  in consistency with the large in-plane linear response.

In Fig. 8 we also show the shift vector integrated over the Brillouin zone  $e\bar{R}^{aa}$  for the monochalcogenides. The integral of the shift vector has been previously studied for complex oxides, such as  $\text{BiTiO}_3$  and  $\text{PbTiO}_3$  in Ref. 5 where no obvious relation was found between the shift vector and the shift current spectra, instead the relation was found to depend on the degree of localization between initial and final states in the optical transitions. On the contrary, in the single-layer monochalcogenides, with delocalized  $p$ -type valence and conduction states, the relation between the shift current spectra and  $e\bar{R}^{aa}$  is pronounced, e.g., the integrated shift vector shows all of the features in  $\sigma$ . This shows that the shift vector clearly drives the shift current response of the monochalcogenides, in other words wavefunction Berry phases play a clear role in the shift current spectra. Following the analysis of Ref. [46] we provide an interpretation of the shift vector in the main text, which complements previous analysis of the shift vector given in Refs. [3, 5, 46].

In Fig. 8 we also show the Glass coefficient,

$$G^{abb}(\omega) = \sigma^{abb}(\omega)/\alpha^{bb}(\omega); \quad (12)$$

where  $\alpha^{bb} = \epsilon^{bb}\omega$  is the absorption coefficient [43]. The Glass coefficient defines the photocurrent of a thick sample (a thick 3D array of slabs in this case) accounting for the incident-light penetration depth ( $\propto 1/\alpha$ ). The calculated  $G^{abb}$  for the single-layer monochalcogenides, of the order of  $\sim 10^{-10}$   $\text{cmAV}^{-2}$ , is relatively large compared to that in prototypical ferroelectric materials, e.g.,  $\sim 10^{-11}$   $\text{cmAV}^{-2}$  in  $\text{BiFeO}_3$  [5] and  $1.3 \cdot 10^{-11}$   $\text{cmAV}^{-2}$  in  $\text{BiTiO}_3$  [5].

### Shift current equivalent in SI

In this section we detail how to convert the shift-current tensor  $\sigma$  to current density generated per unit



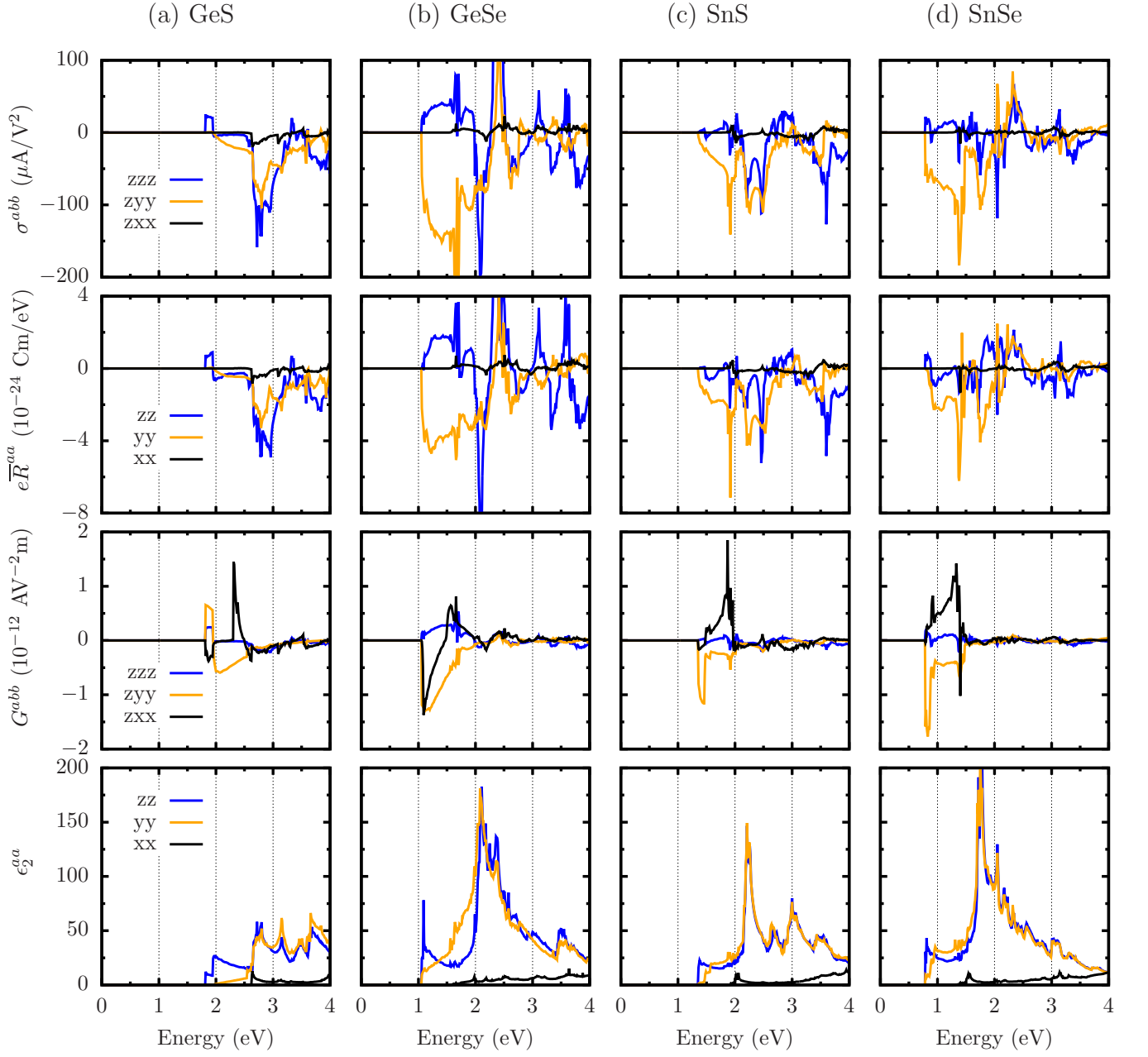


FIG. 8. Shift current spectra, shift vector, linear response and Glass coefficient of single-layer monochalcogenides. The large shift current, Glass coefficient and linear absorption ( $\epsilon_2 \sim 100$ ) induced in the visible range of frequencies indicate their potential for optoelectronic applications.

intensity of light  $\kappa$  in units of  $(\text{A}/\text{m}^2)/(\text{W}/\text{m}^2)$ , and viceversa. We assume a linearly polarized light source of unitary intensity,  $I = c\epsilon_0 E^2/2$ , where  $c$  is the speed of light and  $\epsilon_0$  is the vacuum permitivity. The shift-current respose  $J_{\text{shift}}$  is expressed in terms of the shift-current tensor  $\sigma$  in Eq. 1 of the main text. Hence the current density is,  $\kappa \equiv J_{\text{shift}}/I = 4\sigma/(c\epsilon_0)$ . For example, given a  $\kappa = 400 \text{ mA}/\text{W}$  (at given frequency), say in units of  $(\text{A}/\text{m}^2)/(\text{W}/\text{m}^2) = \text{A}/\text{W}$ , we can convert  $\kappa$  into equivalent units of shift-current tensor.

### Shift current and polarization in the Rice-Mele model

In this section we provide some details of the derivation of the shift current for the one dimensional (1D) Rice-Mele (RM) model. Starting from Eq. (2) in the main text we set  $b = c$  (linear polarization) and using  $r_{nm}^b = |r_{nm}^b|e^{-i\phi_{nm}^b}$  and  $r_{mn;b}^a = \partial r_{mn}^a/\partial k^b - i(A_{nn}^b - A_{mm}^b)r_{nm}^a$ ,

Eq. (2) takes the familiar form

$$\sigma^{abb}(0; \omega, -\omega) = -\frac{\pi e^3}{\hbar^2} \times \int \frac{d^d k}{(2\pi)^d} \sum_{nm} f_{nm} |r_{nm}^b|^2 R_{nm}^{a,b} \delta(\omega_{nm} - \omega), \quad (13)$$

in terms of the shift vector is  $R_{nm}^{a,b} = \partial \phi_{nm}^b / \partial k^a + A_{nn}^a - A_{mm}^a$ . For a two-band model in 1D,  $n, m$  take two values  $c, v$ , and hence we obtain Eq. 6 of the main text. In the derivation we used  $r_{nm}^a = \langle u_n | v^a | u_m \rangle / i\omega_{nm}$  that is valid for non-degenerate bands. Now we apply this results to the RM Hamiltonian Eq. 4. where  $\delta$  parametrizes the dimerization of the chain and  $\Delta$  the staggered on-site potential. Inversion symmetry is broken when  $\delta \neq 0$  and  $\Delta \neq 0$  and preserved otherwise. The unit cell along  $z$ -(of length  $c$ ) has two sites. Since we are interested in a model with the minimal number of parameters that captures the physics of the monochalcogenides, we set the distance between atoms to be the same and modulate only the hopping. We obtain  $\hat{H} = \sum_k (c_{k,A}^\dagger \ c_{k,B}^\dagger) H(k) (c_{k,A} \ c_{k,B})^T$  with Bloch Hamiltonian,

$$H = \sigma_x t \cos(ka/2) - \sigma_y \delta \sin(ka/2) + \sigma_z \Delta \quad (14)$$

and cell periodic functions  $u_n$  such that  $Hu_{c,v} = \pm E u_{c,v}$ . The eigenvalues are given by  $E = \sqrt{t^2 \cos^2 ka/2 + \delta^2 \sin^2 ka/2 + \Delta^2}$  for the conduction and  $-E$  for the valence bands. Berry connections will depend explicitly on the gauge used but the results on the shift vector and shift current are gauge independent. We then compute the shift current and polarization from the Berry connections and velocity matrix elements. If the electric field is along the chain, the  $z$ -direction, the shift current is

$$J_{\text{shift}}^z(\omega) = 2\sigma^{zzz}(0; \omega, -\omega) E^z(\omega) E^z(-\omega). \quad (15)$$

For the two-band model

$$\sigma^{zzz} = e^3 \int_0^{2\pi/a} dk \frac{|\langle u_c | v | u_v \rangle|^2 R_{cv}}{\hbar^2 \omega^2} \delta\left(\frac{2E}{\hbar} - \omega\right) \quad (16)$$

To quantify the amount of shift current generated in short-circuit mode we define the ‘‘average conductivity tensor’’ as,

$$\int d\omega \sigma^{zzz}(0; \omega, -\omega) = e^3 \int dk \frac{|\langle u_c | v | u_v \rangle|^2 R_{cv}}{4E^2} \quad (17)$$

This integral is shown in the main text. It can be expressed analytically in terms of elliptic functions [50]. Here chose model parameters  $(t, [0, \delta_0], \Delta_0) = (1, [0, -.865], .4)$  eV that fit the ab-initio shift current data for GeS. In Fig. 3 in the main text we normalized

	$P_0^{3D}$ (C/m <sup>2</sup> )	$E_g$ (eV)	$\Delta_0/t$	$\delta_0/t$	$\delta_m/t$
GeS	1.9	1.9	0.45	-0.83	-0.52
GeSe	1.3	1.2	0.39	-0.45	-0.45
SnS	0.8	1.4	0.54	-0.52	-0.60
SnSe	0.6	0.9	0.36	-0.20	-0.44

TABLE II. RM model parameters for the 2D monochalcogenides.  $\delta_0$  and  $\Delta_0$  are set to yield the DFT band gap  $E_g$  and the shapes of the polarization curves in Fig. 4 (read text).

the vertical and horizontal axis with respect to the results at the ground state  $(t, \delta_0, \Delta_0) = (1, -.865, .4)$ . For the other monochalcogenides, we estimate the  $\delta_0$  parameter by fitting the DFT direct gap (shown in Table 1 in main text) and the polarization curves shown in Fig. 4, i.e., we solve two equations simultaneously,

$$E_g = \sqrt{\delta_0^2 + \Delta_0^2}$$

$$P_0^{1D} = \frac{1}{2\pi} \int dk A_{vv}(k, \delta_0, \Delta_0) - \frac{1}{2\pi} \int dk A_{vv}(k, 0^+, \Delta_0) \quad (18)$$

We normalize the  $y$  axis in Figs. 4 by  $P_0$ , and then find the best fit of Eqs. 18 properly normalized too. In this way, we obtain the  $\delta$  and  $\Delta$  parameters for the 2D monochalcogenides, shown in Table. II. As mentioned in the main text, for GeS, GeSe and SnS  $\delta_0$  ( $= -0.9, -0.5$  and  $-0.6$  respectively) is relatively close to the optimal  $\delta_m$  of  $-0.5, -0.5$  and  $-0.6$  respectively, whereas for SnSe  $\delta_m$  ( $= 0.4$ ) is farthest from  $\delta_0 = -0.2$ .

TABLE III: Geometry (in Å) of single-layer monochalcogenides used to compute the spontaneous polarization along an adiabatic path connecting  $\mathbf{R}_f^i(\lambda = -1)$  to  $\mathbf{R}_f^i(\lambda = 1)$ , read manuscript.

#### GeS

Lattice parameters:

$$\vec{a} = 15.00 \ 0.00 \ 0.00$$

$$\vec{b} = 0.00 \ 3.66 \ 0.00$$

$$\vec{c} = 0.00 \ 0.00 \ 4.47$$

Atom coordinates:

	$R_0$	$R_f(\lambda = 1.0)$	$R_f(\lambda = -1.0)$
Ge	1.41 0.91 0.00	1.41 0.91 0.59	1.41 0.91 -0.59
Ge	3.97 2.74 2.24	3.97 2.74 2.83	3.97 2.74 1.64
S	3.76 0.91 0.00	3.76 0.91 0.00	3.76 0.91 0.00
S	1.62 2.74 2.24	1.62 2.74 2.24	1.62 2.74 2.24

#### GeSe

$$\vec{a} = 15.00 \ 0.00 \ 0.00$$

$$\vec{b} = 0.00 \ 3.98 \ 0.00$$

$$\vec{c} = 0.00 \ 0.00 \ 4.26$$

Atom coordinates:

	$R_0$	$R_f(\lambda = 1.0)$	$R_f(\lambda = -1.0)$
Ge	1.58 0.99 0.00	1.58 0.99 0.44	1.58 0.99 -0.44
Ge	4.00 2.98 2.13	4.00 2.98 2.58	4.00 2.98 1.68
Se	4.10 0.99 0.00	4.10 0.99 0.09	4.10 0.99 -0.09
Se	1.49 2.98 2.13	1.49 2.98 2.22	1.49 2.98 2.04

#### SnS

Lattice parameters:

$$\vec{a} = 15.00 \ 0.00 \ 0.00$$

$$\vec{b} = 0.00 \ 4.11 \ 0.00$$

$$\vec{c} = 0.00 \ 0.00 \ 4.27$$

Atom coordinates:

	$R_0$	$R_f(\lambda = 1.0)$	$R_f(\lambda = -1.0)$
Sn	1.45 1.03 0.00	1.45 1.03 0.47	1.45 1.03 -0.47
Sn	4.29 3.08 2.13	4.29 3.08 2.61	4.29 3.08 1.66
S	4.04 1.03 0.00	4.04 1.03 0.19	4.04 1.03 -0.19
S	1.71 3.08 2.13	1.71 3.08 2.32	1.71 3.08 1.94

### SnSe

Lattice parameters:

$$\vec{a} = 15.00 \ 0.00 \ 0.00$$

$$\vec{b} = 0.000 \ 4.31 \ 0.00$$

$$\vec{c} = 0.000 \ 0.00 \ 4.38$$

Atom coordinates:

	$R_0$	$R_f(\lambda = 1.0)$	$R_f(\lambda = -1.0)$
Sn	1.58 1.08 0.00	1.58 1.08 0.41	1.58 1.08 -0.41
Sn	4.33 3.23 2.19	4.33 3.23 2.60	4.33 3.23 1.78
Se	4.31 1.08 0.00	4.31 1.08 0.22	4.31 1.08 -0.22
Se	1.61 3.23 2.19	1.61 3.23 2.41	1.61 3.23 1.97